ORIGINAL RESEARCH



Check for updates

Hybrid Photovoltaics cell with triboelectric nanogenerator: Overcoming energy availability limits and reducing optical scattering losses

Ramsundar Sivasubramanian | Chockalingam Aravind Vaithilingam | Suriati Paiman | Ashish Sharma | Indragandhi V | 0

²Center for Sustainable Societies, 1, Jalan Taylor's, Taylor's University Selangor, Subang Jaya, Selangor, Malaysia

³Department of Physics, Faculty of Science, Universiti Putra Malaysia, Serdang, Selangor, Malaysia

⁴Discovery Partners Institute, University of Illinois System, Chicago, Illinois, USA

⁵Department of Climate, Meteorology and Atmospheric Sciences, University of Illinois Urbana-Champaign, Urbana, Illinois, USA

⁶School of Electrical Engineering, VIT, Vellore, India, India

Correspondence

Chockalingam Aravind Vaithilingam, Clean Technology Impact Lab, Taylor's University, Petaling 47500, Malaysia.

Email: aravindcv@ieee.org

Abstract

Solar photovoltaics has long been a major research area in renewable and sustainable energy, with a large percentage of these efforts directed towards resolving PV limitations, the most critical of which is energy availability. The amount of solar PV power output is related to the amount of irradiation incident on it; hence, times of no or low irradiation levels result in zero or reduced power generation. The design and analysis of the optical performance of a contact-separation triboelectric nanogenerator integrated hybrid PV cell that can scavenge energy from rain without interfering with the device's normal operation is presented in this work. The hybrid cell's redesigned materials and structure enable it to minimize optical scattering losses recorded at the top glass layer of conventional PV devices by up to 50% while enhancing transmittivity from 90% to 95% across the visible wavelength range of 400–800 nm.

KEYWORDS

energy availability, hybrid PV cell, optical performance, solar photovoltaics, triboelectric nanogenerator

1 | INTRODUCTION

Solar photovoltaics (PV) technology has been and continues to be one of the most widely used renewable energy sources, and for good reason. Except for production, installation, and disposal, PV panels are essentially a carbon-negative source of clean energy that can be deployed with relatively few limits to harness a natural source of energy (sunlight) that is available practically anywhere on the planet's surface. However, the technology has some limits, particularly in terms of conversion efficiency, energy supply, and reaction to demand changes. Demand fluctuations, for example, can be addressed using intermediate energy storage

During the preparation of this work, the author(s) used Quillbot for language refinement. After using this tool/service, the author(s) reviewed and edited the content as needed and take(s) full responsibility for the content of the publication. and suitable sizing where necessary. Extensive research efforts continue to yield newer generations of solar PV technology with ever-increasing efficiency. The fundamental nature of solar PV, which converts incident solar irradiation into electric potential, can potentially be a major restriction. Solar PV output is hampered by periods of inactivity and reduced performance at night and during periods of reduced sunshine (due to weather events such as overcast sky, rains, etc.). One strategy to address this limitation is to use complementary power generation technologies, which is the logic used in this study. Solar PV cells have been topped with a transparent contact-separation triboelectric nanogenerator capable of capturing energy from rainfall. Because the nanogenerator is transparent, it does not prevent irradiation from reaching the PV surface, allowing both devices to run simultaneously. During rainy seasons, the nanogenerator layer supplemented the PV layer's power output.

¹Clean Technology Impact Lab, 1, Jalan Taylor's, Taylor's University Selangor, Subang Jaya, Selangor, Malaysia

1.1 Scavenging rain energy as a source of energy

Rain has two types of energy: raindrop electrostatic energy, which is caused by the interaction of gaseous molecules in the atmosphere with the droplet as it falls through the atmosphere, and raindrop kinetic energy, which is caused by its mass and velocity. Raindrops range in size from 0.5 to 4 mm and reach a terminal velocity as they fall through the atmosphere, when the drag on the droplet surface balances the force of gravity acceleration on the droplet's mass. When these droplets strike a surface, they impart velocity (mechanical energy) and, if the impact surface is a dielectric, electrostatic charges.^{2,3} For example, the momentum of precipitation on a material could be exploited to gather energy via material characterization. Raindrops range in size from 0.05 to 4 millimeters, as seen in Figure 1.

The difficulty in harnessing rainfall energy stems from its very scattered nature throughout time and location. Following this, there is less exergy and more entropy. However, geographical phenomena such as crop devastation and soil erosion have long demonstrated how the energy of rainfall affects the ecosystem. With developments in material science, nanogenerators have emerged as a viable option for capturing and utilizing this energy.

1.2 Conceptual framework

The conceptual framework is based on the fundamental equations of electromagnetics, as shown in Figure 2, with the contact separation illustratively. Maxwell's whole focus was on developing the theory of electromagnetic waves. To account for the effect of mechanical energy triggering on the medium and even surface charges, an additional term, polarization current P (generally neglected but with material orientation and choice this makes significant value) in the displacement current D due to static charges and the electrical energy εE (constitute for optical energy conversion depending on the material used). This addition of the polarization component to the charge unit's edge boundary includes electromagnetic and polarization coupling.

The rationale behind this study is that one approach to overcoming this difficulty is to employ complementary power producing strategies. Here, solar PV cells are covered with a transparent contact-separation triboelectric nanogenerator that can capture

rainfall energy. The two devices can cooperate since light may still reach the PV surface due to the nanogenerator's transparency. The PV layer's power generation is enhanced by the nanogenerator layer's when it rains. Researchers have made multiple successful attempts to harness this energy using TENGs and PENGs, with some cases including the mechanisms being integrated with other similar renewable energy harvesting methods such as tidal and wind power.⁴⁻⁷

This paper is organized with Section 2 exploring evolution towards hybrid PV cells to accommodate the energy scavenging from the rain drop electrostatic forces, the CSTNG hybrid PV cell, and the analysis of the optical performance of such devices. Section 3 addresses the results and pertinent discussions on the new CSTENG hybrid cell. Finally, Section 4 concludes the paper, summarizing key findings and recommendations.

MATERIALS AND METHODS

Contact-separation nanogenerator operation

TENG employed in this study operated in vertical contact separation mode and is as shown in Figure 3 which illustrates the steps involved in operation.

TENG's top and bottom layers are initially electrically neutral. Once contact was made, the two dielectrics' differing triboelectric potentials caused equal and electrically opposing charges to form on their contact surfaces. When the layers begin to separate, the triboelectric surface charges induce opposing charges on the electrode (conductor) layers adhered to them. Because the two electrodes are connected by an external circuit, electrons flow through it to neutralize the charge in the electrode layers, resulting in a pulse of current in the external circuit.^{8,9} Although the charges in the electrode are neutralized by the flow of electrons through the external circuit, the charges created in the dielectric layers remain due to the limited/nil charge mobility in dielectric materials. When the distance between these two charged dielectric layers begins to change in the following stage as the TENG layers approach each other, they behave like a capacitor and cause a current to flow in the external circuit, this time in the opposite direction due to the switched layer polarity. As a result, when the process repeats in a cycle, the CS-TENG produces an alternating current output^{1,2}



FIGURE 1 Rain droplets of various shapes and sizes.

19447450, 0, Downloaded from https://aiche.onlinelibrary.wiley.com/doi/10.1002/ep.70046 by University Of British Columbia, Wiley Online Library on [01/09/2025]. See the Terms and Conditional Conditi

onditions) on Wiley Online Library for rules of use; OA articles are governed by the applicable Creative Commons

FIGURE 2 Electro-static force and the concept of triboelectricity in CS TENG.

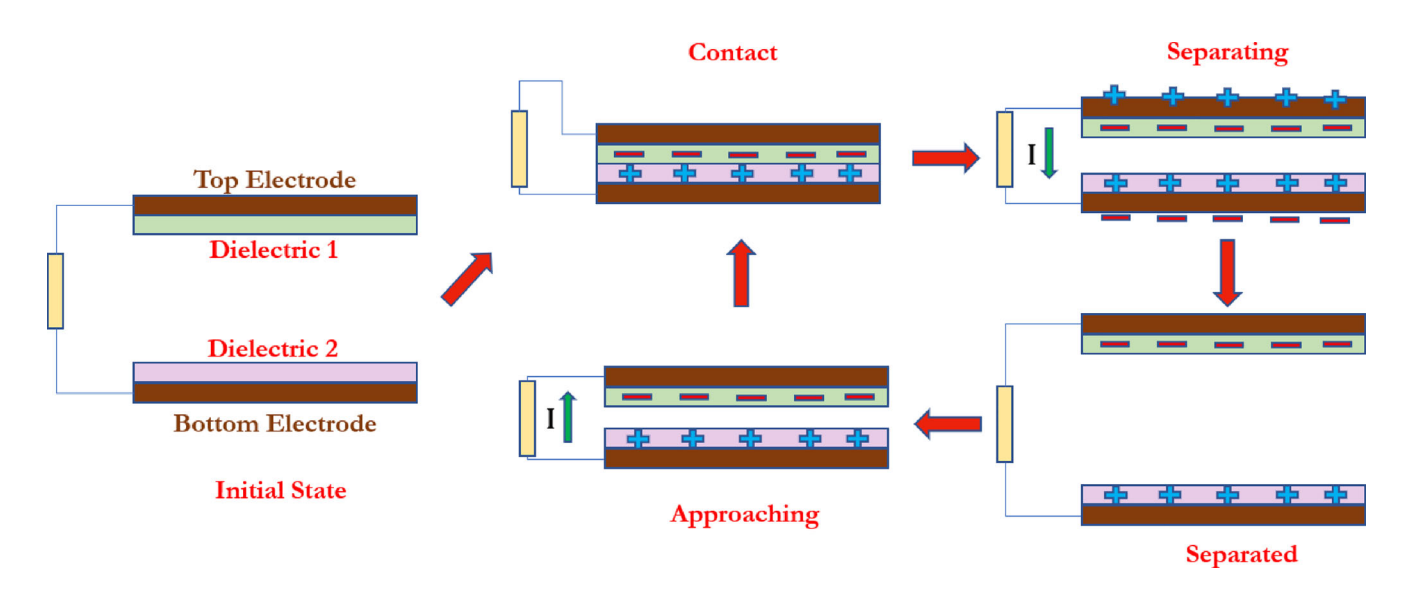


FIGURE 3 Contact Separation TENG-steps of operation.

2.2 | Electrical model

A CS-TENG can be modeled as a parallel plate capacitor that operates according to Gauss' law since the TENG surface (capacitor plate) area is significantly bigger than the separation distance between the TENG layers. In this case, the assumptions of electric fields aligned normal to the dielectric plane and uniform charge distribution throughout the entire surface area apply. The voltage (V) between the electrodes is calculated as the sum of the electric fields across the dielectrics ε_1 and ε_2 of the plates and ε_0 the air gap dielectric, and the separation distance (between d_1 and d_2) as 10,11 in Equation (1).

$$V = -\frac{Q}{S\varepsilon_o} \left(\frac{d_1}{\varepsilon_1} + \frac{d_2}{\varepsilon_2} + x(t) \right) + \frac{\sigma x(t)}{\varepsilon_o}$$
 (1)

where, x(t) is the time dependent separation distance between the TENG layers with thicknesses d_1 and d_2 and relative permittivities ε_1 and ε_2 respectively; σ is the surface charge density, S is the TENG (surface) area and Q is the electrode charge.

For a TENG consisting of two electrode backed dielectric layers operating in the vertical contact separation mode at constant velocity (v), the resultant short circuit current (I_{sc}) is given by the relation as in Equation (2).

$$I_{sc} = \frac{S\sigma v d_o}{\left(d_o + x(t)\right)^2} \tag{2}$$

where, $d_o = \frac{d_1}{\varepsilon_1} + \frac{d_2}{\varepsilon_2}$

The open circuit voltage (V_{oc}) is given by Equation (3),

$$V_{oc} = \frac{\sigma x(t)}{\varepsilon_o} \tag{3}$$

For the constant velocity condition, the velocity (v) is calculated as in Equation (4)

$$v = \frac{2(x_{max} - x_{min})}{T} \tag{4}$$

where, x_{max} and x_{min} are the maximum and minimum separation distances between the dielectric layers respectively and T is the duration of one cycle of TENG contact separation operation.

2.3 | CS-TENG PV hybrid cell

The proposed hybrid cell architecture consists of the following layers: glass at the bottom, followed by PV rear electrodes, then the semiconductor layer, and finally top electrodes. The layers preceding this component make up the hybrid cell's PV subsystem. The triboelectric nanogenerator component is made up of two polymeric films: fluorinated ethylene propylene (FEP) and polydimethylsiloxane (PDMS), which are physically separated by a spacer and have electrodes

stacked on planar sides that do not face each other. The bottom polymeric layer and the superior layer of the PV cell share a common electrode. The top electrode can be copper or, for improved optical performance, any transparent conducting oxide, such as the most widely used Indium Tin Oxide. Raindrops hitting the hybrid cell's highest layer/surface cause contact separation between the two polymeric layers. This causes the two layers to develop a potential difference due to the varying propensities of the two constituent materials to lose or gain electrons (as indicated by their position in the triboelectric activity series) and become polarized, gaining opposing electrical charges with respect to each other. These polarized charges are neutralized by the passage of electrons through electrodes layered on the layers, which are then routed through an external circuit. This procedure represents the electrical power output of the hybrid cell's triboelectric nanogenerator component. The electrodes on the top triboelectric layer were engineered to mimic those on the PV surface below to eliminate shading losses caused by metallic electrodes. 12 The polymeric layers were chosen to achieve a balance of maximum triboelectric polarization capacity and optical transmittivity. This assured that the resulting nanogenerator assembly had equivalent or higher optical transmittivity than the standard glass top layers in PV panels. Figure 4 is a depiction of the proposed CS-TENG-PV hybrid cell, including the constituent layers.

2.4 | Material selection for the CS-TENG

The proposed CS-TENG architecture in this study was created using four different materials: three dielectrics and one electrically conductive substance. The most important material selection criteria for this work were applied to the selection of the dielectrics that would constitute the two layers of the CS-TENG. The triboelectric series is an ordered collection of materials based on their triboelectric potentials. A material's triboelectric potential is essentially a measure of its tendency to lose (tribo-positive) or gain (tribo-negative) electrons through polarization when it encounters another dielectric or conductive material. A TENG can be built using any two dielectric materials with distinct triboelectric potentials.

However, to get the highest TENG performance, the selected materials must have as large a triboelectric potential difference as possible. ^{5,6} In the case of the proposed design in this study, because the CS-TENG had to be developed to function as part of a hybrid cell integrated with a photovoltaic cell rather than as a standalone device, various other factors/constraints enter the triboelectric materials selection. According to the proposed device design in the preceding section, because the TENG is layered on top of the PV cell, strong optical transmittivity of the TENG layers is critical.

The values must be equivalent to or larger than the standard tempered glass covers found in traditional PV modules/cells. This constraint eliminated various types of triboelectric materials, such as rubbers, wood, crystalline polymers, and some organic materials, because they are not optically transparent despite their great triboelectric performance. The second important aspect was material durability—because

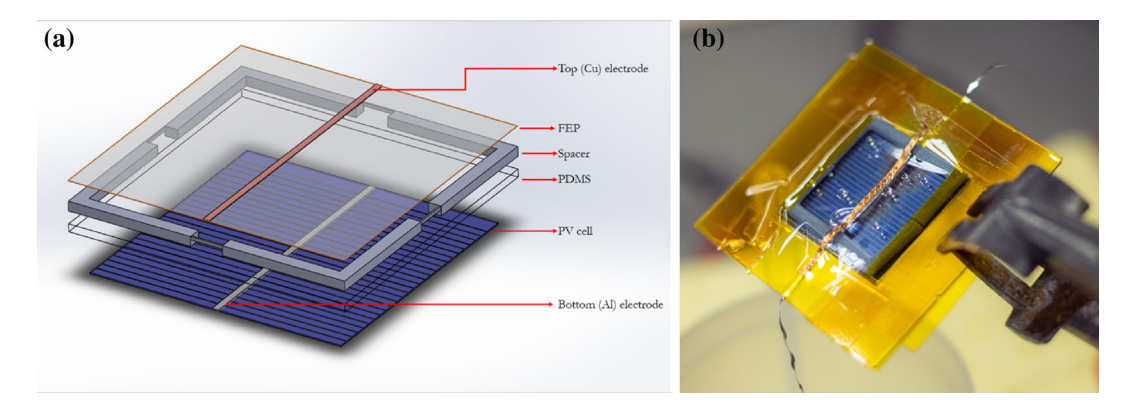


FIGURE 4 CS-TENG PV hybrid cell: the exploded view and the prototype.

the TENG's object of integration is a PV cell, the materials utilized must have service durations equal to those used in commercial solar panels, which have an average service life of 20–25 years. ^{13–15} This implies a requirement for materials with well-documented weathering qualities and resilience against environmental pollutants.

The third criterion to examine was the successful completion of the contact-separation action using the chosen driving force—raindrops in this example. The material used for the top TENG layer must have the appropriate elastic modulus so that the deflection caused by raindrop impact is at least equal to or slightly more than the layer separation distance in the TENG. Given all these considerations, fluorinated ethylene propylene (FEP) and polydimethylsiloxane (PDMS) were chosen as the dielectric materials for the CS-TENG. The top CS-TENG layer was made of FEP, which is the more tribonegative of the two materials, while the bottom layer was made of PDMS, which is tribo-positive in comparison.

2.4.1 | Fluorinated ethylene propylene

Fluorinated ethylene propylene is a highly flexible polymer with numerous industrial applications. It is highly valued for its optical transparency, ¹⁶ mechanical durability, ^{11,17} outstanding weathering characteristics, ^{12,18} and chemical stability, ^{13,19} which has led to its employment in a wide range of applications, ^{14,20} including the performance and lifetime enhancement of optical and electronic systems. ^{15,21} FEP has a high contact angle (112°–120°) with water, making it more hydrophobic than polyvinyl fluoride (PVF) or glass, ^{16,22} which are commonly used facing materials in conventional PV modules.

This feature also makes FEP appealing for solar PV applications since it makes the PV cells/modules more resistant to contamination from environmental causes, allowing the hybrid cell to remain clean for longer periods of time than a PV cell coated in glass. The mechanical and thermal durability of FEP and its excellent resistance to UV degradation have been well documented in the literature. ²³ In addition, the superior hydrophobic nature of FEP also enables it to have good triboelectric charge retention properties, particularly when used for solid-liquid contact electrification applications. ²⁴

This investigation used Dupont Teflon clear FEP films, Type A (general use variation). It is an amorphous polymer composed of tetra-fluoroethylene and hexafluoropropylene. Because of its amorphous form, FEP is both transparent and isotropic. It has low permeability to organic vapors, gases, moisture, and liquids, and it is chemically inert and resistant to almost all chemical substances except for very uncommon ones such as gaseous fluorine, complex halogenated compounds, and molten alkali metals, all of which are unlikely to be present in the Hybrid cell's expected operational environments.

2.4.2 | Polydimethylsiloxane

PDMS is an amorphous, dielectric silicone oil or resin that, when mixed with a curing agent, forms an elastomer through crosslinking. The ratio of resin to curing agent utilized determines the qualities of the final elastomer, such as hardness and elasticity. This elastomer is particularly effective in infiltrating and flowing into small areas, and after curing, it easily preserves even micro-meter scale mold characteristics, making it a preferred choice for microlithography and micro electro-mechanical systems (MEMS) applications.²⁵ Because PDMS is biocompatible, it is useful in a variety of biomedical and biotechnological applications.²⁶ Due to its ease of use, diversity in fabrication, and strong triboelectric properties, PDMS is frequently employed in nanogenerators of diverse sizes and morphologies.^{27,28}

PDMS is also very transparent, resistant to a variety of environmental pollutants, and hydrophobic. The polymer is made up of a lengthy chain of siloxane groups that end with silanol groups. In this study, Dow Sylgard 184 resin and hardener were employed to create the PDMS film for the CS-TENG.

2.4.3 | FEP-PDMS triboelectric mechanism

While section 1.3 outlined the basic operating principle of a CS-TENG, with the top dielectric material being more tribo-negative than the bottom one, this section will go over the mechanism of surface charge production between the two dielectrics during contact separation.

FEP is made up of several highly polar C-F (carbon-fluorine) covalent bonds, with the F end being significantly more electronegative than the C end. As a result, the overall —CF3 and —CF2— groups along the polymeric chain have negative charges oriented towards the F atoms and slightly positive ends. In the absence of an external electric field, the groups are randomly distributed across the material, making it electrically neutral.

On the other hand, PDMS is made up of numerous methyl (CH3-) groups connected by a lengthy chain of —Si—O— bonds. Normally, the methyl groups are non-polar, but the presence of electronegative —Si—O— groups attracts the molecule's negative charges, leaving the methyl groups slightly positively charged. Like FEP, these charges are randomly oriented in the absence of an electric field, and the material is electrically neutral.

When the two dielectrics come into contact, interfacial polarization occurs because the negative C-F groups in the FEP and the positive methyl groups in the PDMS attract each other, resulting in a concentration of electrical charges along the interfacial boundaries in each dielectric. This results in an opposing charge on the other border of the dielectric material in contact with the metallic electrode. Even after the two dielectrics split, their limited charge mobility allows them to retain polarized charges for longer periods of time than metallic electrodes, which are neutralized by the passage of electrons through the external circuit. The entire cycle is repeated each time the two dielectric layers of the CS-TENG are driven to contact each other repeatedly.

2.5 | Optical performance of the hybrid cell via ray-tracing studies

The hybrid cell's geometry was designed in a modeling tool and then analyzed through Monte Carlo ray-tracing simulations in TracePro (by Lambda Research Corporation). To mimic sun irradiation in the simulation space, the appropriate optical parameters (reflectivity, absorptivity, and transmittivity) were defined for each layer in the hybrid cell model, as shown in Table 1, as well as a light source (grid source, random pattern with solar divergence angle). Ray-tracing studies were carried out on a hybrid cell with a footprint of 40 mm \times 40 mm to compare the results to lab-based physical tests. The findings of the ray-tracing analyses were presented as irradiation maps,

allowing the study of the effects of the interfering triboelectric nanogenerator layers on the overall optical behavior of the hybrid cell. The analyses were performed under different irradiance levels, and the findings were compared to the simulated optical performance of a typical PV cell with the same device footprint and conditions. Figure 5 depicts a few instances of typical irradiation maps derived from ray-tracing investigations.

A ray independence test was used to ensure that the number of rays from the light source defined in the Monte-Carlo ray tracing model had no effect on the results. The same model geometry was reproduced with similar test conditions by altering simply the number of rays emerging from the light source. Ray counts ranged from 100,000 to 4,000,000. The lowest ray count value at which the average irradiance values on the target surface stabilized was used in further analyses. The proposed hybrid cell was also compared to a regular PV cell model with a similar device footprint to investigate the implications of incorporating the CS-TENG layers on top of the PV cell. Table 1 shows the different layers in each model and their average transmittivities over the visible wavelength range.

Ray tracing simulations were run for three incidence conditions: fixed cell with normal incidence, uniaxial tracking, and dual axis tracking. The study's geographic coordinates were 3° 04′ 18.00″ N, 101° 35′ 16.79″ E, which corresponds to Taylor University's Lakeside campus in Subang Jaya, Malaysia. The simulations for the three incidence circumstances were repeated for the hybrid and standard PV cell models, respectively.

For the uniaxial tracking condition cases, the cell models were set at a 3° inclination along the north-south axis (with the edge of the cells facing north being higher) to ensure maximum irradiance on the cell by matching the inclination with the latitude value, as is standard practice in solar PV setups. Every simulation using both tracking setups for both cell models was run from 6 a.m. to 8 p.m., with irradiance data captured every thirty minutes. This period corresponds to a duration that is somewhat longer than the time the sun would be above the horizon at that place. Furthermore, the date of June 21, 2024, was picked for study, which corresponds to the summer solstice to ensure that the studies were done on a date with maximal daylight hours at the chosen geographic location. The solar source for both tracking and normal incidence was adjusted to a standard

TABLE 1 Layers of the hybrid cell and standard PV cell models.

Hybrid cell			Standard PV cell		
Layer	Average optical transmittivity [%]	Thickness [mm]	Layer	Average optical transmittivity [%]	Thickness [mm]
FEP	96	0.05	Top glass	89	3
PLA Spacer	92 ³	1.5	Encapsulant (top)	92	1
PDMS	92	1	PV cell	0 (target surface)	0.128
PV cell	0 (target surface)	0.128	Encapsulant (bottom)	92	1
Glass substrate	89	3	Backsheet	0	0.1
Top electrode (Copper)	0	0.1			
Top electrode (ITO)	85 ⁴	0.1			

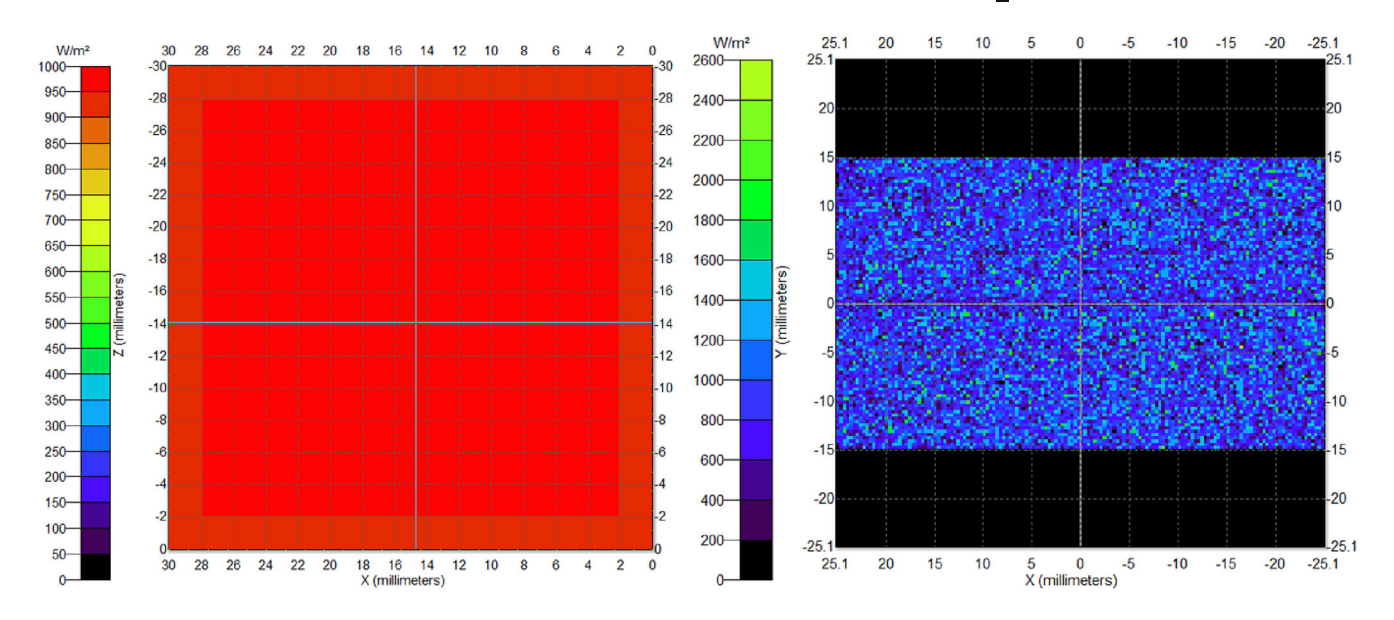


FIGURE 5 Irradiation maps ray-tracing analyses of the PV hybrid cell.

irradiance value of 1000 Wm⁻² and a sun distance of 300 mm. For the purposes of this study, which was primarily concerned with observing the impacts of the superseding layers on the PV cell layer in the models, the effects of atmospheric and sky models on solar irradiance were ignored. Once the source was configured, the remaining system parameters for the tracking simulations, such as the model and workspace orientation, solar path trajectory calculation, entrance pupil size, location, and orientation in the model space, model rotational axis for tracking, and tracking tolerance in degrees, were set accordingly. Tracking tolerances of 0, 1, and 5 degrees were explored to reflect the effects of tracking inaccuracies in real-world scenarios due to mechanical/hardware constraints. A halogen PAR (parabolic aluminium reflector) light array was utilized in conjunction with an interior testing setup to compare the hybrid cell's performance to that of a traditional PV with a tempered glass cover. Both cells were tested at similar irradiance levels, and their output voltages were recorded. A UV-Vis spectroscope (Shimadzu UV-1900i) was used to investigate the transmittance spectra of the TENG polymeric layers (FEP and PDMS) over a wavelength range of 300-1100 nm. A slow scan speed was employed at 0.1 nm intervals, and each scan was repeated three times before the resulting data was averaged to get the final set of measurements. The spectrometer light source fluctuations were avoided by collecting each reading only after the warm-up phase had ended. The transmittance spectrum data was analyzed to compare the performance of CS-TENG layers with traditional tempered glass in PV panels/cells.

2.6 | Testing the CS-TENG layer under water droplet impact

To test the performance of the TENG layer of the hybrid cell, an experimental setup to mimic the impact of rain drops on the cell was

assembled using a burette on a height-adjustable clamp and stand with a leveled sample stage placed underneath the nozzle center. Distilled water was used to negate the effects of particulate impurities and was dripped onto the sample placed below the burette at a controlled rate. The respective TENG outputs for different water dripping rates were then recorded to determine the optimum TENG actuation rate from the water (rain) droplets.

3 | RESULTS AND DISCUSSION

3.1 | Transmission spectra for the CS-TENG layers

Figure 6 shows the transmission spectra graph for the CS-TENG layers versus a common type of optical glass (N BK-7 Schott; transmission spectra including Fresnel reflection at interfaces; Source—Schott catalogue data for N BK-7).

Figure 6a depicts an overview of the transmittance spectra for the CS-TENG layers (FEP and PDMS) versus the spectra for high clarity optical glass (NBK-7; Schott). Figure 6b displays a magnified view of the area of interest, which is the visible spectrum between 400 and 800 nm. The spectra demonstrate that both FEP and PDMS have greater average transmittance over the visible spectrum. FEP has the best performance (\sim 95%), followed by PDMS (\sim 93%), and finally glass (\sim 91%), which has the comparatively poorest transmittance.

As a result of these findings, CS-TENG composed of these polymeric layers will allow for greater irradiance incidence on the PV cell as compared to glass, resulting in improved solar performance. Another point to consider is that the tempered glass commonly used in PV applications has a rough textured bottom surface to improve bonding with the EVA encapsulant; however, because this surface roughness is on a much larger scale than the wavelength of visible light, it causes additional scattering/reflection of incident radiation

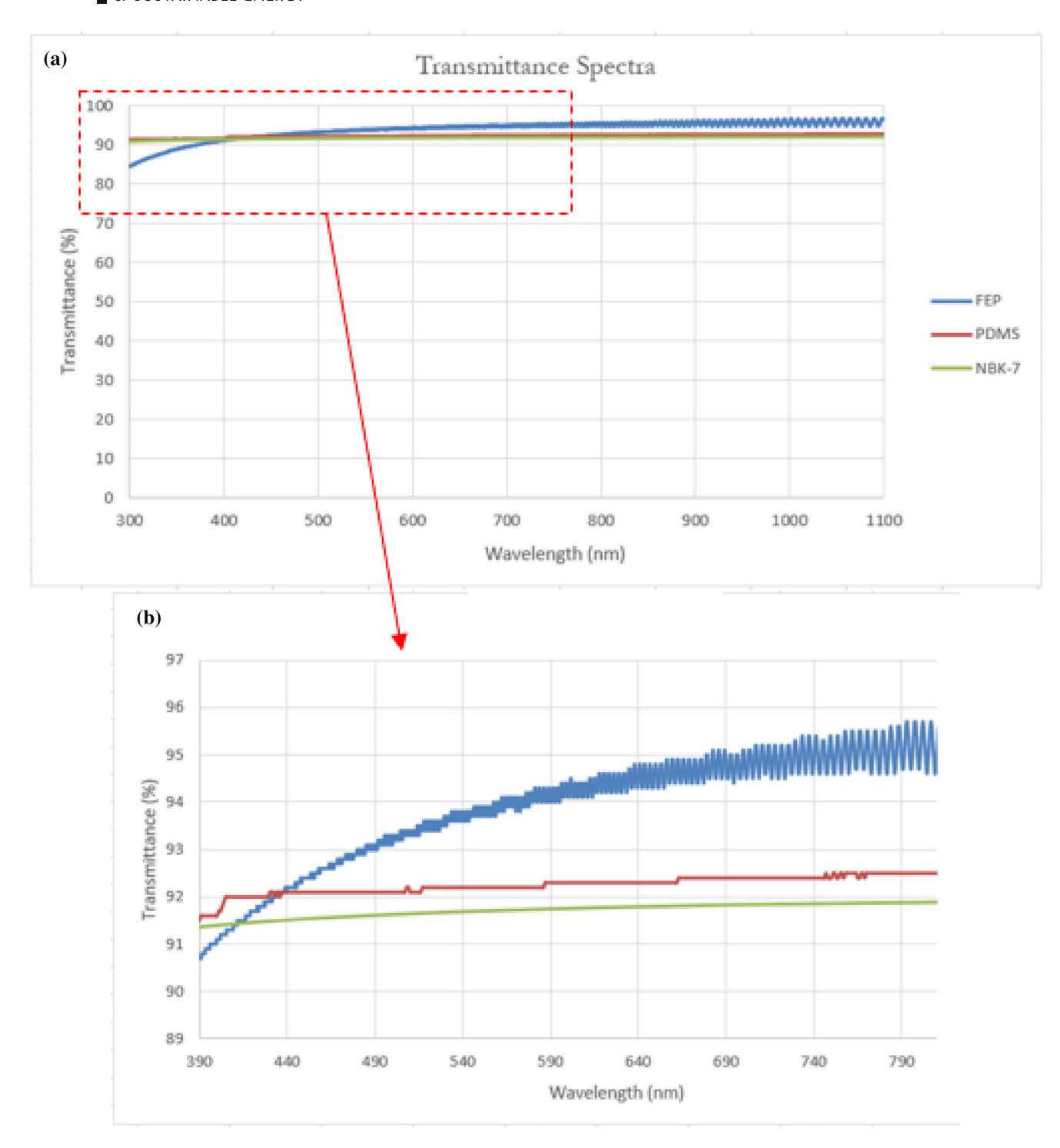


FIGURE 6 (a) Transmittance spectra for the CS-TENG layers versus glass (NBK-7 Schott). (b) magnified view of the same spectra (visible light range)

and thus more losses, lowering the net effective transmittance to 88%-89%.²⁹ In the case of cast PDMS, the surface roughness tends to be in the same range as the wavelength of light, reducing optical losses by imparting an anti-reflective feature to the air-polymer interface. Using the largest feasible difference in transmittance values results in a maximum 5% decrease in optical losses in terms of net incident irradiance, or a 50% reduction in losses when compared to using glass (considering N BK-7 glass as the baseline) over PV cells/ panels.

This optical performance is on par with other anti-reflective strategies currently in the market such as micro-textured glass, 30 ceramics 31 and nano-textured polymeric films 32 which can improve the transmittivity by up to 5% (i.e., 95% transmittivity). 33 But certain coatings among these types with micro-porosities on the surface, such as SiO_2 or TiO_2 ceramic coatings, necessitate the use of additional hydrophobic coatings to tackle their propensity for soiling because of their originally low water surface contact angles (hydrophilic surface).

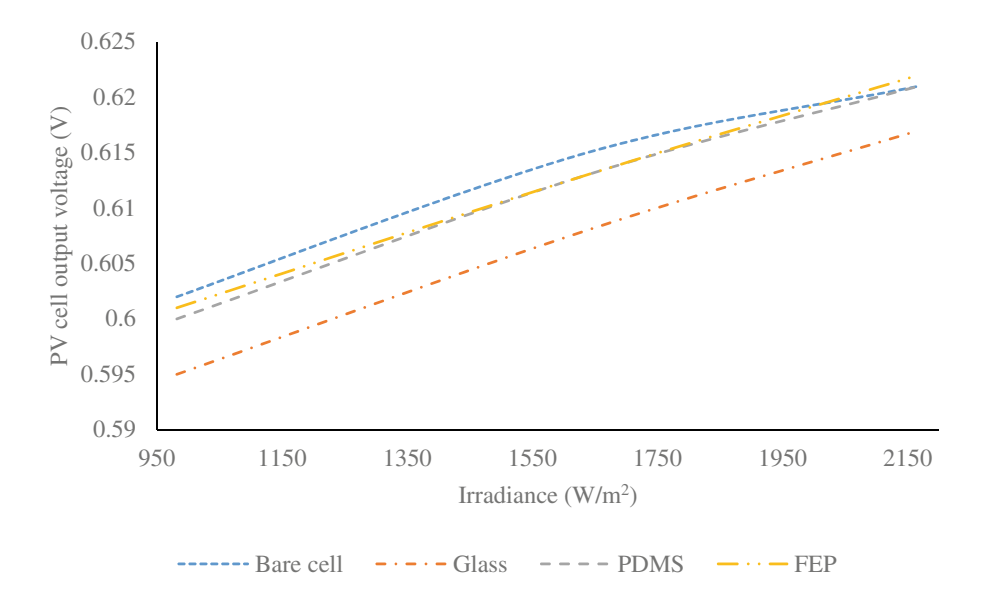


FIGURE 7 Electrical output (V) of PV cell versus irradiance for varying overlaid media.

This tendency for soiling can negate any potential power gains in the PV from the anti-reflective properties.³² On the other hand, using materials such as FEP, as proposed in this study, obviates the need for an additional anti-soiling layer and integrates both anti-reflective and anti-soiling properties into a single layer, thus resulting in cost and material savings.

3.2 | Variation in PV output versus different covering media

As described in Section 2.3, PV cells were covered with various media and their output was tested under identical irradiance conditions. The test cases included bare cells, cells with FEP, cells with PDMS, and cells with a tempered glass cover. The findings are presented in Figure 7.

The graph's results reveal that, omitting the bare cell, the FEP coated cell had the highest output, followed by PDMS with only a marginal difference, and finally the glass coated cell with the lowest output, which differed significantly from the previous two examples. The data here followed a similar trend to the transmission spectra, supporting the notion that higher transmittance values result in increased PV production. The naked cell in this case was a control setup, which showed a marginally superior performance compared to the cells coated with the polymers, but that is to be expected because in that case the complete irradiance from the light source was incident without obstruction on the PV cell.

3.3 | Ray-tracing results

3.3.1 | Ray independence test

The ray independence test results are displayed in the graph below (Figure 8). The graph shows that 1,000,000 was the lowest ray count at

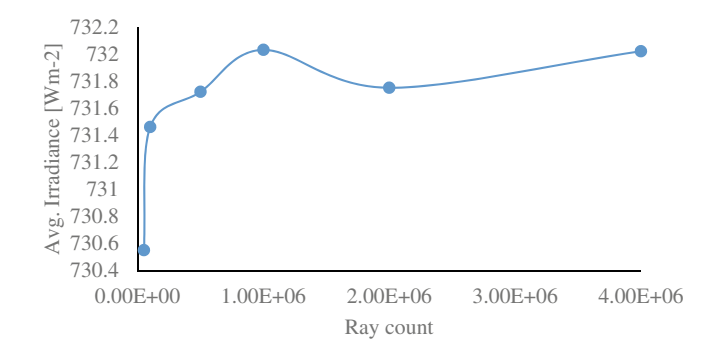


FIGURE 8 Graph illustrating the results of the ray independence test.

which the average irradiance values from the ray tracing simulations remained steady; hence, it was used for all further investigations.

3.3.2 | Optical performance of cell models under normal incidence condition

Figure 9 shows the results of the ray tracing studies for regular PV cells and CS-TENG-PV hybrid cells side by side. Both devices have the same footprint and were subjected to the same irradiation conditions in the simulation setting. The data shows that the hybrid cell, with both a totally opaque top electrode and an optically transparent ITO electrode, has a higher overall flux incident on the PV layer than a standard PV setup with a glass cover. This is due to the CS-TENG layers' better overall transmittance as compared to glass and encapsulant in the standard PV cell type. Clearly, the cell model with the transparent ITO electrode had the highest incident irradiance on the PV layer, followed by the hybrid cell model with an opaque top electrode, and finally the normal PV model. An unexpected result was that, despite the shading losses caused by an opaque top electrode in the

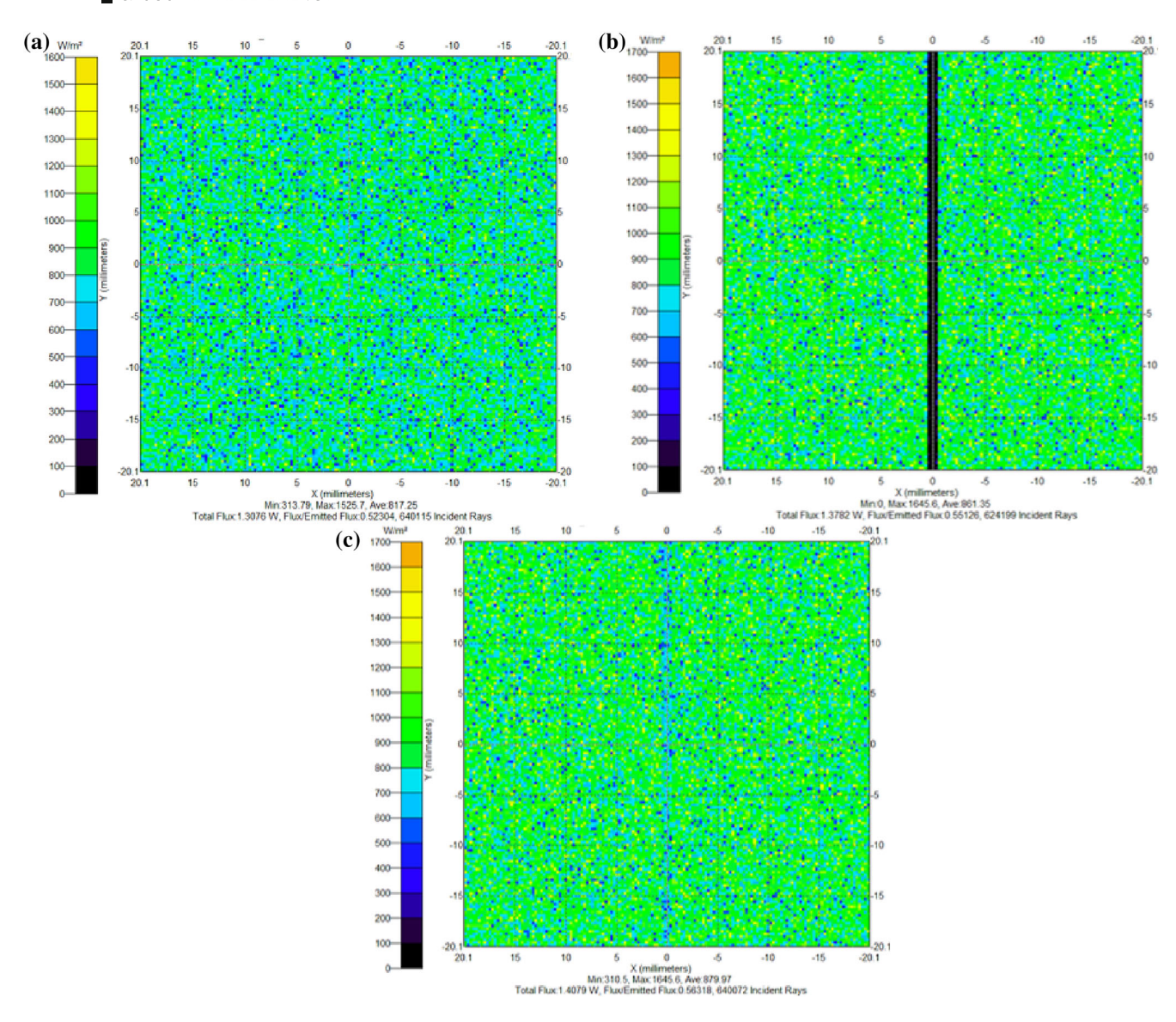


FIGURE 9 Ray-tracing results for conventional PV versus CSTENG-PV hybrid cell. (a) standard PV cell model (b) hybrid cell with opaque top electrode (c) hybrid cell with ITO top electrode.

cell, the higher total transmittance more than compensated for the loss in irradiance. Hence, both cases of hybrid cell models showed superior performance to the regular cell model.

Furthermore, in the proposed design, the glass layer was moved to the bottom of the assembly, keeping its benefits of providing structural stability to the hybrid cell while also making the design more suitable for bifacial PV configurations. Another advantage of replacing the glass at the top with polymeric CS-TENG layers is that the hybrid cell gains hydrophobic properties, which boosts its resistance to fouling and allows it to work for longer periods of time between cleaning procedures. The top layer's hydrophobicity ensures that any liquid that meets the cell rolls off, as well as any dust or debris that has accumulated on the surface. The largest difference in flux computed per unit area from the ray-tracing data between the three cases was 62.72 Wm⁻², which is a significant gain over standard PV panels, given that PV panels have power densities of 200–300 Wm⁻².

3.3.3 | Optical performance of cell models under tracking conditions

Figure 10 shows a plot of the net flux collected versus time for both cells (standard and hybrid) under uniaxial and dual-axis tracking scenarios.

3.4 | Performance of the CS-TENG

This section compares the practically documented results of the CS-TENG performance from this work to the performance of an S-TENG model from the literature created for the same goal—to scavenge energy from rain. For this goal, Zheng et al.'s³⁴ work was used as a point of contrast. Like this effort, the chosen literature described a concept for a silicon PV cell—TENG hybrid cell that can harness

power from both sunshine and rain. The key difference between the two investigations was the TENG design chosen: the comparison study employed an S-TENG, whereas the current study used a CS-TENG. As stated in the literature review summary, using an S-TENG only allowed for the capture of raindrop electrostatic energy, whereas a CS-TENG could harness both electrostatic and kinetic energies, as mentioned in the research hypothesis and design description. Thus, by using this work as a reference, the benefits of a CS-TENG over an S-TENG for raindrop energy collecting could be clearly demonstrated. Figure 11 illustrates the variation in TENG output current and voltage as load resistance changes for the reference literature and the current investigation.

Both the reference study and the current work showed similar output voltage and current density profiles under varied load situations. The voltage climbed slowly at first with rising load resistance, but then increased dramatically after a certain transition point beyond 1E6 ohms. The current density curve behaved similarly, but the trend was inverted, with a high starting value at low resistance and then a decrease with rising resistance.

The greatest power point for the TENG in both bases was seen at the intersection of the voltage and current density curves. Though the overall trend was comparable in both cases, the absolute values of current density and voltage for the current work were higher than in the reference study. This could be ascribed to the CS-TENG's greater efficiency energy conversion mechanism, which included both the raindrop electrostatic and kinetic energies, as opposed to the S-TENG, which only used the electrostatic energy component. The operational parameters for the hybrid cell in the current investigation were a droplet dripping height of 0.6 m at a frequency of 8 drops/second and a per droplet diameter of 1.79 mm. The TENG output for the

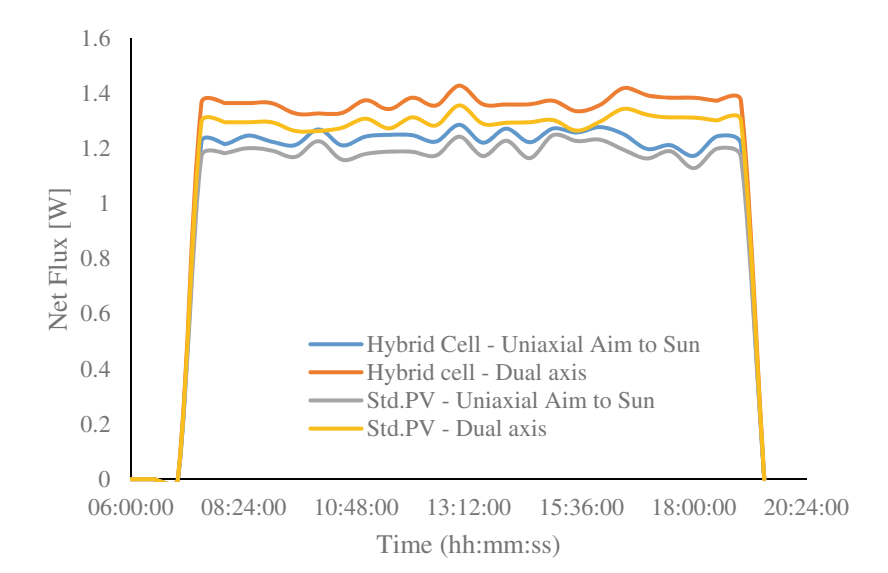
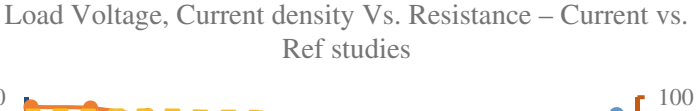


FIGURE 10 Graph of the net flux [W] versus time for the two cell models under two tracking scenarios.



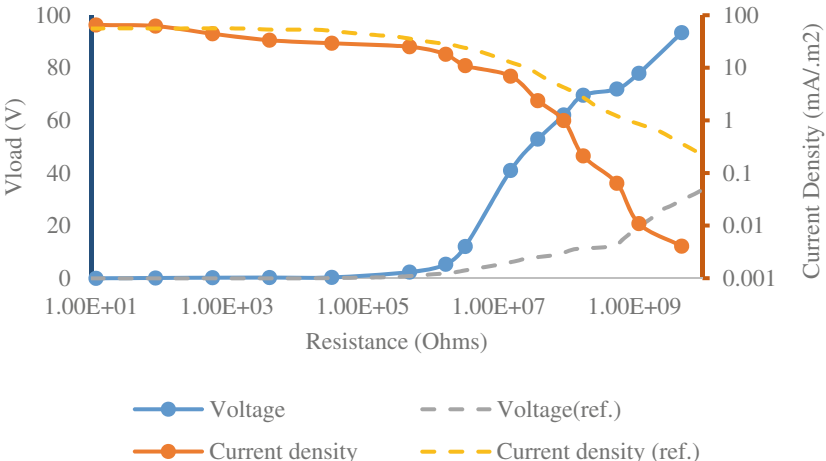


FIGURE 11 Output voltage and current density against varying load³⁴ versus current study.

19447450, 0, Downloaded from https://aiche

elibrary.wiley.com/doi/10.1002/ep.70046 by University Of British Columbia, Wiley Online Library on [01/09/2025]. See the Terms

on Wiley Online Library for rules of use; OA articles

governed by the applicable Creative Commons

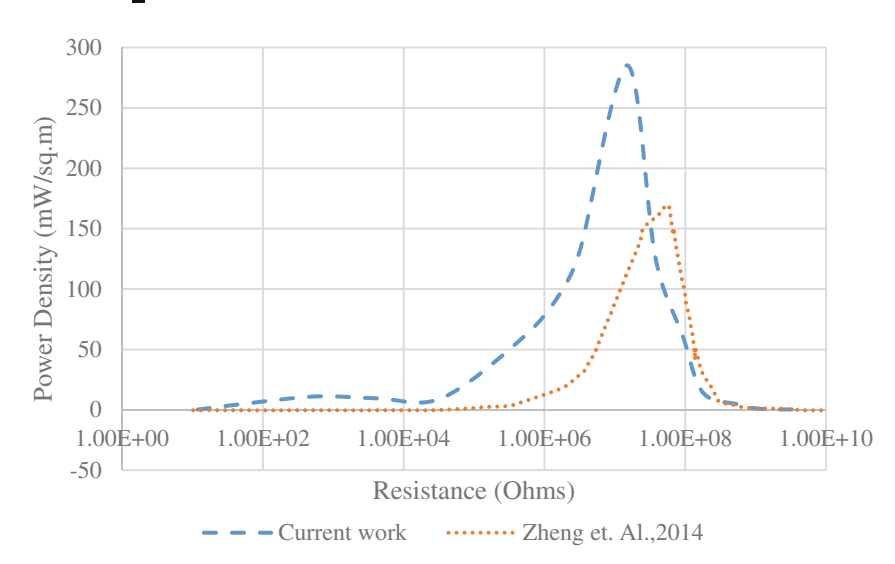


FIGURE 12 Power density plots comparing the TENG performance under varying load.

reference study was obtained under the operational parameters of a 0.116 mL/s water discharge rate. Figure 12 shows a graph of the power density plots of both TENGs under varying load. The graph above shows the clear performance difference between the CS-TENG from this study and the S-TENG in the reference literature. Peak power density values of 285 mW/m² and 170 mW/m² were recorded for the CS-TENG and S-TENG, respectively. This increase in power density of around 67% over the S-TENG highlighted the clear benefit of deploying a CS-TENG for raindrop energy gathering.

As evidenced by the disparities in power densities between the TENG and PV components of the hybrid cell, the CS-TENG only plays a supplemental role in the hybrid cell while the PV component remains the primary power source. The small-scale output from the TENG serves as a value addition to PV during times of rainfall when solar irradiation and consequently PV output is negligible. The TENG layers improve the PV performance by reducing scattering, as discussed in the earlier sections, while its power output is sufficient for applications such as LED lighting, IoT-based sensors/devices for smart applications, similar to other cases in the literature. 35,36

CONCLUSION

The results of the investigation show that the suggested CS-TENG-PV hybrid cell has significant advantages over conventional PV technology. The main benefits include reducing optical losses by up to 50% compared to the original value.

- The polymeric layers' hydrophobic nature prevents fouling from environmental contaminants.
- The hybrid cell uses both solar radiation and rain droplets without negatively impacting PV performance.

The main takeaway from this study's findings was that the proposed CS-TENG-PV hybrid cell model outperformed a standard PV

model in terms of optical performance while also opening an avenue for energy scavenging from rain, which complements solar PV technology's environmentally friendly features. Even though the data presented here show the promising prospects of the proposed hybrid cell model, the nascent expectations must be tempered, as certain aspects of the design still require further investigation and testing before it can compete with conventional PV technology on a commercial basis. The primary issues are cost, longevity, the effect on solar PV's net carbon footprint, and manufacturing technologies for commercial-scale production. Other methods of improving the TENG performance, such as increasing the surface charge retention of the dielectrics via the inclusion of metal-organic frameworks (MOFs)^{37,38} or through the inclusion of hole and electron blocking layers³⁹ can also be considered to improve the overall performance of the hybrid cell design.

CONFLICT OF INTEREST STATEMENT

None of the authors have a conflict of interest to disclose.

DATA AVAILABILITY STATEMENT

The data that support the findings of this study are available on request from the corresponding author. The data are not publicly available due to privacy or ethical restrictions.

ORCID

Chockalingam Aravind Vaithilingam https://orcid.org/0000-0002-

Indragandhi V https://orcid.org/0000-0003-0351-7761

REFERENCES

- 1. Sivasubramanian R, Vaithilingam CA, Indira SS, Paiman S, Misron N, Abubakar S. A review on photovoltaic and nanogenerator hybrid system. Mater Today Energy. 2021;20:100772. doi:10.1016/j.mtener. 2021.100772
- 2. Jiuqin Y, Yin L, Longxi C. Preliminary study on mechanics-based rainfall kinetic energy. Int Soil Water Conserv Res. 2014;2:67-73. doi:10. 1016/S2095-6339(15)30024-1

- Lam HY, Din J, Jong SL. Statistical and physical descriptions of raindrop size distributions in equatorial Malaysia from Disdrometer observations. Adv Meteorol. 2015;2015:1-14. doi:10.1155/2015/ 253730
- Zheng L, Cheng G, Chen J, et al. A hybridized power panel to simultaneously generate electricity from sunlight, raindrops, and wind around the clock. Adv Energy Mater. 2015;5:1501152. doi:10.1002/aenm. 201501152
- Jeon S-B, Kim D, Yoon G-W, Yoon J-B, Choi Y-K. Self-cleaning hybrid energy harvester to generate power from raindrop and sunlight. Nano Energy. 2015;12:636-645. doi:10.1016/j.nanoen.2015. 01.039
- Jung S, Oh J, Yang UJ, et al. 3D Cu ball-based hybrid triboelectric nanogenerator with non-fullerene organic photovoltaic cells for selfpowering indoor electronics. *Nano Energy*. 2020;77:105271. doi:10. 1016/j.nanoen.2020.105271
- Yang H, Wang M, Deng M, et al. A full-packaged rolling triboelectricelectromagnetic hybrid nanogenerator for energy harvesting and building up self-powered wireless systems. *Nano Energy*. 2019;56: 300-306. doi:10.1016/j.nanoen.2018.11.043
- Zheng M, Lin S, Tang Z, Feng Y, Wang ZL. Photovoltaic effect and tribovoltaic effect at liquid-semiconductor interface. *Nano Energy*. 2021; 83:105810. doi:10.1016/j.nanoen.2021.105810
- Born M, Wolf E, Bhatia AB, et al. Principles of Optics: Electromagnetic Theory of Propagation, Interference and Diffraction of Light. 7th ed. Cambridge University Press; 1999. doi:10.1017/CBO9781139644181
- Callaty C, Gonçalves I, Rodrigues C, Ventura J. Modeling the performance of contact-separation triboelectric nanogenerators. *Curr Appl Phys.* 2023;50:100-106. doi:10.1016/j.cap.2023.03.013
- Niu S, Wang S, Lin L, et al. Theoretical study of contact-mode triboelectric nanogenerators as an effective power source. *Energy Environ* Sci. 2013;6:3576. doi:10.1039/c3ee42571a
- Sripadmanabhan Indira S, Vaithilingam CA, Sivasubramanian R, Chong K-K, Saidur R, Narasingamurthi K. Optical performance of a hybrid compound parabolic concentrator and parabolic trough concentrator system for dual concentration. Sustain Energy Technol Assess. 2021;47:101538. doi:10.1016/j.seta.2021.101538
- Ellinas K, Gogolides E. Ultra-low friction, superhydrophobic, plasma micro-nanotextured fluorinated ethylene propylene (FEP) surfaces. Micro Nano Eng. 2022;14:100104. doi:10.1016/j.mne. 2022100104
- Ebnesajjad S, Khaladkar PR. Manufacturing Parts from Melt-Processible Fluoropolymers In Plastics Design Library Fluoropolymer Applications in the Chemical Processing Industries. William Andrew Publishing; 2018: 219-277. doi:10.1016/B978-0-323-44716-4.00006-3
- Sibin KP, Swain N, Chowdhury P, et al. Optical and electrical properties of ITO thin films sputtered on flexible FEP substrate as passive thermal control system for space applications. Sol Energy Mater Sol Cells. 2016;145(3):314-322. doi:10.1016/j.solmat.2015.10.035
- Sebastian D, Yao C-W, Lian I. Mechanical durability of engineered superhydrophobic surfaces for anti-corrosion. *Coatings*. 2018;8(5): 162. doi:10.3390/coatings8050162
- Jiang Z, Guo Z, Jia Z, Xiao C, An S. Chemical stability of novel melt spinning FEP fibers. E-Polymers. 2016;16(2):171-176. doi:10.1515/ epoly-2015-0252
- Sibin KP, Srinivas G, Shashikala HD, et al. Highly transparent and conducting ITO/Ag/ITO multilayer thin films on FEP substrates for flexible electronics applications. Sol Energy Mater Sol Cells. 2017;172: 277-284. doi:10.1016/j.solmat.2017.08.001
- Samuels SL, Glassmaker NJ, Andrews GA, Brown MJ, Lewittes ME. Teflon FEP frontsheets for photovoltaic modules: Improved optics leading to higher module efficiency, 2010 35th IEEE Photovoltaic Specialists Conference, IEEE, Honolulu, HI, USA. 2010: pp. 2788– 2790. doi:10.1109/PVSC.2010.5616754

- Lee S, Park J-S, Lee TR. The wettability of fluoropolymer surfaces: influence of surface dipoles. *Langmuir*. 2008;24:4817-4826. doi:10. 1021/la700902h
- Bhayat MH, Vaithilingam CA, Oruganti KSP, Sivasubramanian R, Ardhanari J. Monofacial and bifacial photovoltaics systems with uniaxial solar tracking. J Phys Conf Ser. 2023;2523:012024. doi:10.1088/ 1742-6596/2523/1/012024
- Atkinson PJ, Fleming RJ. Thermally stimulated conductivity in electron irradiated FEP-Teflon Conference on Electrical Insulation & Dielectric Phenomena—Annual Report Boston USA. 1980. 337–344. doi:10.1109/EIDP.1980.7683863
- Singh A, Umakanth V, Tyagi N, Kumar S. A comparative study of different polymer materials for the development of flexible crystalline silicon modules. Sol Energy Mater Sol Cells. 2023;255:112259. doi:10.1016/j.solmat.2023.112259
- Im S, Frey E, Lacks DJ, Genzer J, Dickey MD. Enhanced triboelectric charge stability by air-stable radicals. Adv Sci. 2023;10:2304459. doi: 10.1002/advs.202304459
- Extrand CW. The use of fluoropolymers to protect semiconductor materials. J Fluor Chem. 2023;122(1):121-124. doi:10.1016/S0022-1139(03)00103-9
- Galante AMS, Galante OL, Campos LL. Study on application of PTFE, FEP and PFA fluoropolymers on radiation dosimetry. *Nucl Inst Methods Phys Res A*. 2010;619(1–3):177-180. doi:10.1016/j.nima. 2009.10.103
- Yoshikawa K, Kawasaki H, Yoshida W. Silicon heterojunction solar cell with interdigitated back contacts for a photoconversion efficiency over 26%. Nat Energy. 2017;2:17032.
- Janssen GJM, Tool CCJ, Kossen EJ, van Aken BB, Carr AJ, Romijn IG.
 Aspects of bifacial cell efficiency Energy Procedia, Proceedings of the 7th International Conference on Silicon Photovoltaics SiliconPV. 2017.
- Dziedzic J, Inglot M. Ultrathin glass for the photovoltaic applications.
 Acta Phys Pol A. 2017;132:176-178. doi:10.12693/APhysPolA.
 132.176
- Law AM, Jones LO, Walls JM. The performance and durability of antireflection coatings for solar module cover glass—a review. Sol Energy. 2023;261:85-95. doi:10.1016/j.solener.2023.06.009
- 31. Zambrano-Mera DF, Espinoza-González R, Villarroel R, et al. Optical and mechanical properties of Zr-oxide doped TiO2/SiO2 anti-reflective coatings for PV glass covers. Sol Energy Mater Sol Cells. 2022;243:111784. doi:10.1016/j.solmat.2022.111784
- Elsafi A, Aïssa B, Ilse K, Abdallah A. Performance and durability of anti-soiling and anti-reflective coatings for photovoltaic systems in desert climates. Sol Energy. 2025;293:113446. doi:10.1016/j.solener. 2025.113446
- Huh D, Choi H-J, Byun M, Kim K, Lee H. Long-term analysis of PV module with large-area patterned anti-reflective film. *Renew Energy*. 2019;135:525-528. doi:10.1016/j.renene.2018.12.055
- Zheng L, Lin Z-H, Cheng G, et al. Silicon-based hybrid cell for harvesting solar energy and raindrop electrostatic energy. *Nano Energy*. 2014;9:291-300. doi:10.1016/j.nanoen.2014.07.024
- 35. Potu S, Madathil N, Mishra S, et al. Surface-engineered high-performance triboelectric nanogenerator for self-powered health monitoring and electronics. ACS Appl Eng Mater. 2023;1:2663-2675. doi:10.1021/acsaenm.3c00416
- Bochu L, Potu S, Navaneeth M, Khanapuram UK, Rajaboina RK, Kodali P. Innovative integration of triboelectric nanogenerators into signature stamps for energy harvesting, self-powered electronic devices, and smart applications. *Engineering*. 2024;5:958-966. doi:10. 3390/eng5020052
- 37. Sun X, Dong L, Liu J, et al. Regulating contact electrification and charge retention capability with metal-organic frameworks in triboelectric nanogenerator for self-powered sewage treatment. *Adv Funct Mater.* 2025;35:2422803. doi:10.1002/adfm.202422803

- 38. Babu A, Gupta S, Katru R, et al. From acoustic to electric: advanced triboelectric nanogenerators with Fe-based metal-organic frameworks. *Energ Technol*. 2024;12:2400796. doi:10.1002/ente. 202400796
- Firdous I, Fahim M, Daoud WA. Performance enhancement of triboelectric nanogenerator through hole and electron blocking layersbased interfacial design. *Nano Energy*. 2021;82:105694. doi:10.1016/ j.nanoen.2020.105694

How to cite this article: Sivasubramanian R, Vaithilingam CA, Paiman S, Sharma A, V I. Hybrid Photovoltaics cell with triboelectric nanogenerator: Overcoming energy availability limits and reducing optical scattering losses. *Environ Prog Sustainable Energy*. 2025;e70046. doi:10.1002/ep.70046